

# Insight into the Redox Reaction Heterogeneity within Secondary Particles of Nickel-Rich Layered Cathode Materials

Jiyang Li, Jingxin Huang, Hongyang Li, Xiangbang Kong, Xue Li,\* and Jinbao Zhao\*

Cite This: *ACS Appl. Mater. Interfaces* 2021, 13, 27074–27084

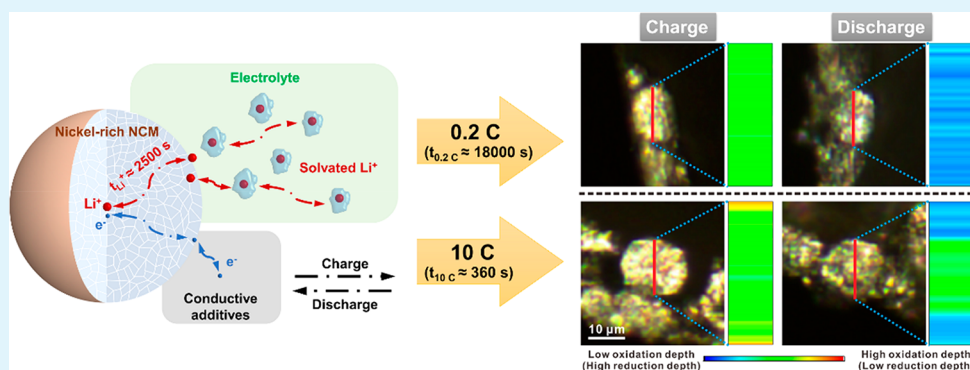
Read Online

ACCESS |

Metrics &amp; More

Article Recommendations

Supporting Information



**ABSTRACT:** Nickel-rich  $\text{LiNi}_x\text{Co}_y\text{Mn}_{1-x-y}\text{O}_2$  (nickel-rich NCM,  $0.6 \leq x < 1$ ) cathode materials suffer from multiscale reaction heterogeneity within the electrode during the electrochemical energy storage process. However, owing to the lack of appropriate diagnostic tools, the systematic understanding and observation on the redox reaction heterogeneity at the individual secondary-particle level is still limited. Raman spectroscopy can not only reflect the depth of the redox reaction through probing the vibrational information on the metal–oxygen coordination structure but also sensitively detect the local structure changes of different regions within the secondary particle with suitable spatial resolution. Therefore, Raman spectroscopy is applied here to conveniently conduct the high-resolution and in-depth analysis of the rate-dependent reaction heterogeneity within nickel-rich NCM secondary particles. It is found that, under high-rate conditions, the oxidation/reduction reaction mainly occurs in the surface region of the particles and the cause of this particle-scale reaction heterogeneity is the limitation of the slow solid-phase  $\text{Li}^+$  diffusion and the transient charging/discharging processes. In addition, this reaction heterogeneity would aggravate the structural instability of the material continuously during the charging/discharging cycles, thus resulting in a slowdown in the kinetics of  $\text{Li}^+$  de/intercalation and the apparent capacity decay. This work can not only provide fundamental insight into the rational modification of high-power nickel-rich NCM materials but also guide the setting of electrochemical operating conditions for high-power lithium-ion batteries (LIBs).

**KEYWORDS:** nickel-rich NCM cathode, rate-dependent, reaction heterogeneity, structural stability, kinetic degradation

## 1. INTRODUCTION

With the rapid development of the electric vehicle market, the requirements for the energy and power density of lithium-ion batteries (LIBs) are steadily increasing.<sup>1–4</sup> At present, nickel-rich  $\text{LiNi}_x\text{Co}_y\text{Mn}_{1-x-y}\text{O}_2$  (nickel-rich NCM,  $0.6 \leq x < 1$ ) materials have been regarded as one of the most promising cathode materials with high energy/power density, which is attributed to their high capacity and the low cobalt content.<sup>5–7</sup> However, in practical operation, there still exist many problems leading to the performance degradation of nickel-rich NCM materials (e.g., surface reconstruction, oxygen release, dissolution of transition metal ions, mechanical microcracks, poor thermal stability, and terrible storage performance).<sup>8–14</sup> In fact, another important but often neglected factor for the performance degradation is the reaction heterogeneity, which can be mainly attributed to the following factors. (i) In terms of

material preparation, due to the polycrystalline property and secondary-particle morphology, the inhomogeneous distribution of the transition metal elements (Ni, Co, Mn) within the materials would result in the heterogeneous redox reaction during the electrochemical charging/discharging process.<sup>15–18</sup> (ii) In the aspect of the  $\text{Li}^+$  diffusion inhomogeneity, the solid-phase  $\text{Li}^+$  diffusion in the cathode material is generally regarded as the rate-limiting step of the half-battery reaction.<sup>19–23</sup> In the process of energy storage, the difference

Received: March 29, 2021

Accepted: May 26, 2021

Published: June 4, 2021



in the diffusion rate of lithium ions will cause the heterogeneous reaction, especially under high-rate conditions. (iii) In the aspect of composite electrodes, owing to the complexity of the composition, the mismatch of the local ionic/electronic conductivity can cause the reaction heterogeneity between different particles at the electrode level.<sup>24–28</sup> The multiscale reaction heterogeneity would further lead to the inhomogeneous distribution of the state of charge (SOC) and stress at the electrode/particle level, thus accelerating the deterioration of the structure and electrochemical performances of the material. Therefore, it is urgent to systematically investigate the reaction heterogeneity in order to deeply understand the degradation mechanism of nickel-rich NCM materials and guide the modification research.

At present, researchers have made efforts to understand the reaction heterogeneity from multiscale perspectives. At the macro scale, Cha et al. proposed that, due to the overutilization of the active materials at the surface side, the nickel-rich NCM particles suffer from reaction heterogeneity in the vertical direction of the electrode surface, causing the inhomogeneous distribution of SOC.<sup>28</sup> By means of fast time-resolved in situ X-ray diffraction (XRD), Zhou et al. reported the rate-dependent phase transition processes of  $\text{LiNi}_{1/3}\text{Co}_{1/3}\text{Mn}_{1/3}\text{O}_2$  during the fast charging processes and found that the intermediate phase between the H1 and H2 phases emerged at high rates ( $>10$  C) and is closely related to the inhomogeneous distribution of SOC in materials.<sup>29</sup> At the micro scale, Xu et al. observed an apparently heterogeneous SOC distribution in a single  $\text{LiCoO}_2$  particle at the high rate by means of in situ transmission X-ray microscopy (TXM).<sup>30</sup> With the help of synchrotron X-ray tomography, Xia et al. quantified the morphological characteristics of the microcracks inside the  $\text{LiNi}_{1/3}\text{Co}_{1/3}\text{Mn}_{1/3}\text{O}_2$  secondary particle after cycling at the high rate, and then associated them with the heterogeneous SOC distribution on the secondary-particle surface.<sup>31</sup> Moreover, through transmission electron microscopy (TEM), Hwang et al. reported the differences in the “layered-spinel rock salt” phase transition between the bulk and surface structure of the  $\text{LiNi}_{0.4}\text{Co}_{0.3}\text{Mn}_{0.3}\text{O}_2$  and  $\text{LiNi}_{0.8}\text{Co}_{0.1}\text{Mn}_{0.1}\text{O}_2$  primary particles at the high rate (10 C).<sup>32</sup> Ko et al. also observed the heterogeneous chemical and structural degradation within the nickel-rich NCM primary particle through electron energy loss spectroscopy (EELS).<sup>12</sup> All of the above studies provide useful information for the in-depth understanding of the multiscale reaction heterogeneity inside the cathode. As is known to all, commercial NCM materials are mainly microscale polycrystalline materials composed of secondary particles. However, because of the limitations of the current research, the reaction heterogeneity within the individual nickel-rich NCM secondary particle remains poorly understood. (i) In the aspect of structural information, as one of the current commonly used testing methods, XRD is conducive to the analysis of long-range ordered crystal structures and is not sensitive to short-range local structures, while X-ray tomography is only suitable for reflecting the morphological information (crack, porosity, specific surface area, etc.) inside the material. (ii) In the spatial resolution respect, the signals measured by XRD are averaged over the structural information on a large number of secondary particles at the electrode scale, and the sample area detected by the electron-related techniques is usually nanoscale within the primary particle, which is not suitable for investigating a single secondary particle with a diameter of several micrometers. (iii) In terms of convenience, the X-ray-based techniques need the

support of a synchrotron radiation light source,<sup>33</sup> and the electron-based techniques require an ultrahigh-vacuum environment and special sample preparation. Therefore, there is still a lack of convenient diagnostic tools which can achieve the high-resolution depth profiling of the reaction heterogeneity within the secondary particle.

Different from the X-ray/electron-based techniques, Raman spectroscopy is very suitable for the investigation of the reaction heterogeneity within the nickel-rich NCM secondary particle for the following reasons. (i) It can capture the correct structural information: as a vibrational spectroscopy, Raman spectroscopy can reflect the redox reaction depth of the nickel-rich NCM materials during  $\text{Li}^+$  de/intercalation by keenly detecting the vibrational characteristics of the metal–oxygen coordination structure.<sup>34–36</sup> (ii) It possesses the appropriate spatial resolution: the spatial resolution of Raman spectroscopy is  $\sim 1$   $\mu\text{m}$ , and the penetration depth of the laser to the nickel-rich NCM material is  $\sim 200$  nm, which enables Raman spectroscopy to obtain the structural information on different local regions within the secondary particle.<sup>37,38</sup> (iii) It can detect conveniently: neither a special excitation source nor a controlled atmosphere is necessary, and the analysis is damage-free under careful excitation conditions.<sup>39</sup> (iv) It can achieve in-depth analysis of particle-scale reaction heterogeneity: through combining the ultramicrotomy technique and Raman imaging, the distribution of the reaction heterogeneity inside the secondary particle can be observed directly.<sup>38,40–42</sup> In a word, based on the advantages of Raman spectroscopy, this work aims to systematically measure the reaction heterogeneity within the nickel-rich NCM secondary particle at different charging/discharging rates and further investigate its impact on the structure and cycle stability. The relevant results obtained can not only guide the modification research of the nickel-rich NCM materials with high power density but also provide favorable suggestions for the electrochemical operating conditions of high-power LIBs.

## 2. EXPERIMENTAL SECTION

**2.1. Structural Characterization.** The nickel-rich NCM material was provided by Beijing Easpring Material Technology Co., Ltd. (China). A Plasma-1000 inductively coupled plasma atomic emission spectrometer (ICP-AES) (NCS, China) was applied to confirm the elemental composition of the nickel-rich NCM material. The morphology and the energy-dispersive spectroscopy (EDS) mapping of the material were measured by a TM3030 scanning electron microscope (SEM) (Hitachi Corporation, Japan). The microstructure of the material was captured by a G2 F30 transmission electron microscope (TEM) (Tecnai, U.S.A.). A Rigaku Miniflex 600 (Rigaku, Japan) was used for the XRD measurements. The Raman spectroscopy measurements used an XploRa confocal microscopic Raman spectrometer (Horiba, Japan). The 532 nm laser was focused on the material particle through a 50 $\times$  objective lens with a working distance of 8 mm. The spatial resolution was  $\sim 1$   $\mu\text{m}$ , and the skin depth of the laser was  $\sim 200$  nm for nickel-rich NCM materials.<sup>34,35,37</sup> The laser power was set to as low as  $\sim 100$   $\mu\text{W}$  to avoid damaging the sample.<sup>43</sup> Raman imaging used the “line scanning” mode with a step length of 400 nm.

**2.2. Preparation and Treatment for the Electrodes.** The nickel-rich NCM material, acetylene black, and poly(vinylidene fluoride) (PVDF) were uniformly dispersed in *N*-methyl pyrrolidone (NMP) with a mass ratio of 8:1:1. Then, the slurry was coated on aluminum foil, dried at 80  $^\circ\text{C}$  for 12 h in a vacuum oven, and punched into wafers to obtain the nickel-rich NCM electrodes. The CR2016 coin cell was assembled with the nickel-rich NCM electrode, a separator (Celgard 2400), electrolyte (1 M  $\text{LiPF}_6$ , EC/DMC = 1:1),

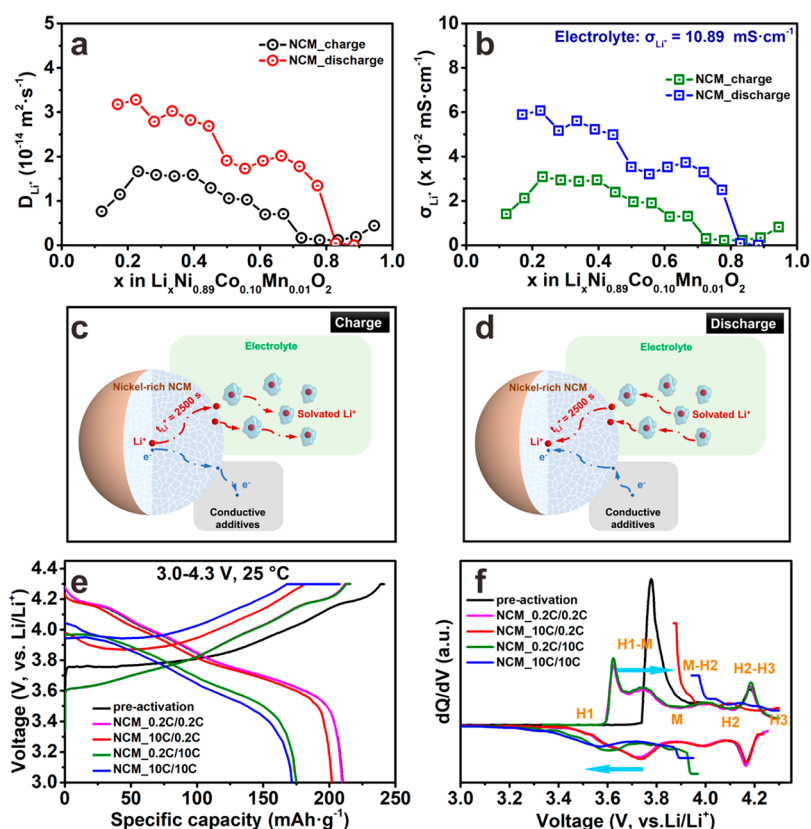


**Figure 1.** (a) Solid-phase  $\text{Li}^+$  diffusion coefficient and (b) lithium ionic conductivity of the nickel-rich NCM material during the charging/discharging process. (c and d) Schematic diagrams of  $\text{Li}^+$  diffusion in the secondary particle. (e and f) The capacity–voltage curves and their corresponding differential capacity curves of the material during the initial cycle in the voltage region of 3.0–4.3 V at different charging/discharging rates.

and the Li counter electrode in an argon-filled glovebox. The cycled nickel-rich NCM electrodes were taken out of the coin cells, rinsed with dimethyl carbonate (DMC), and dried in an argon-filled glovebox. The material particles were cut by an ultrathin microtome (LeicaEMUC7, Germany) to expose the cross sections. To eliminate the possibility of the reaction between the charged materials and the oxygen in air, the Raman spectroscopy measurements used a spectral cell to seal the samples in an argon atmosphere and the XRD measurements used polyimide tape for sealing.

**2.3. Electrochemical Measurement.** The nickel-rich NCM coin cells were operated in the voltage region of 3.0–4.3 V at 25 °C by a LAND CT-2001A battery testing system, which consisted of a constant-current and constant-voltage charging step and a constant-current discharging step. The tests were performed at the charging/discharging rates of 0.2 C/0.2 C for the first cycle and 0.2 C/0.2 C, 0.2 C/10 C, 10 C/0.2 C, and 10 C/10 C (1 C = 180  $\text{mA}\cdot\text{g}^{-1}$ ) for the subsequent cycles, respectively. The galvanostatic intermittent titration technique (GITT) measurement was performed in the voltage region of 3.0–4.3 V with a pulse current density of 18  $\text{mA}\cdot\text{g}^{-1}$  and a pulse time of 10 min, followed by an interval relaxation time of 2 h. The electrochemical impedance spectroscopy (EIS) measurements were performed at 25 °C in the frequency range of 100 kHz to 0.01 Hz by a Solartron SI 1287/1260 electrochemical workstation. Fully charged nickel-rich NCM coin cells after 10 and 50 cycles at different charging/discharging current densities were tested.

### 3. RESULTS AND DISCUSSION

The elemental composition of the nickel-rich NCM material confirmed by ICP-AES is  $\text{Li}/\text{Ni}/\text{Co}/\text{Mn} = 1.05:0.89:0.10:0.01$ . The XRD profile in Figure S1a indicates that the nickel-rich NCM material has a typical  $\alpha\text{-NaFeO}_2$  layered structure belonging to the  $R\bar{3}m$  space group.<sup>8,11</sup> The SEM image in

Figure S1b shows that the secondary particles of the material are nearly spherical with an average diameter of 12  $\mu\text{m}$ . As detected by EDS in Figure S1, parts c and d, the intensity of the transition metal ions (Ni, Co, Mn) is uniform in the radial direction of the cross section, indicating a homogeneous structure composition of the pristine particle.

The possibility of the particle-scale reaction heterogeneity under different charging/discharging rates is qualitatively evaluated based on GITT measurements, which indicates that the heterogeneous reaction within the secondary particle would occur under the high-rate condition (10 C) rather than the low-rate one (0.2 C). First, in Figure 1, parts a and b, the solid-phase  $\text{Li}^+$  diffusion coefficient ( $D_{\text{Li}^+}$ ) and the lithium ionic conductivity ( $\sigma_{\text{Li}^+}$ ) of the nickel-rich NCM material are calculated by the GITT measurement. It is found that the  $\text{Li}^+$  diffusion in the solid phase of the nickel-rich NCM material ( $D_{\text{Li}^+} \approx 1.42 \times 10^{-14} \text{ m}^2\cdot\text{s}^{-1}$ ,  $\sigma_{\text{Li}^+} \approx 2.63 \times 10^{-2} \text{ mS}\cdot\text{cm}^{-1}$ ) is much slower than that in the liquid phase of electrolyte ( $\sigma_{\text{Li}^+} \approx 10.89 \text{ mS}\cdot\text{cm}^{-1}$ ). The specific calculation process is presented in Figure S2. Second, as reported by previous studies, the  $D_{\text{Li}^+}$  of the material is independent of the charging/discharging rate but is determined by the intrinsic structural characteristic of the material itself.<sup>44,45</sup> So the average diffusion time of  $\text{Li}^+$  ( $t_{\text{Li}^+}$ ) from the bulk to the surface in a 12  $\mu\text{m}$  diameter particle under different rates can be estimated based on the average  $D_{\text{Li}^+}$  ( $t_{\text{Li}^+} \approx \frac{R^2}{D_{\text{Li}^+}}$ ), which is approximately 2500 s. As shown in Figure 1, parts c and d, comparing  $t_{\text{Li}^+}$  with the charging/discharging time at different rates ( $t_{0.2 \text{ C}}$  and  $t_{10 \text{ C}}$ ), it is speculated that lithium ions may have enough time to de/intercalate between

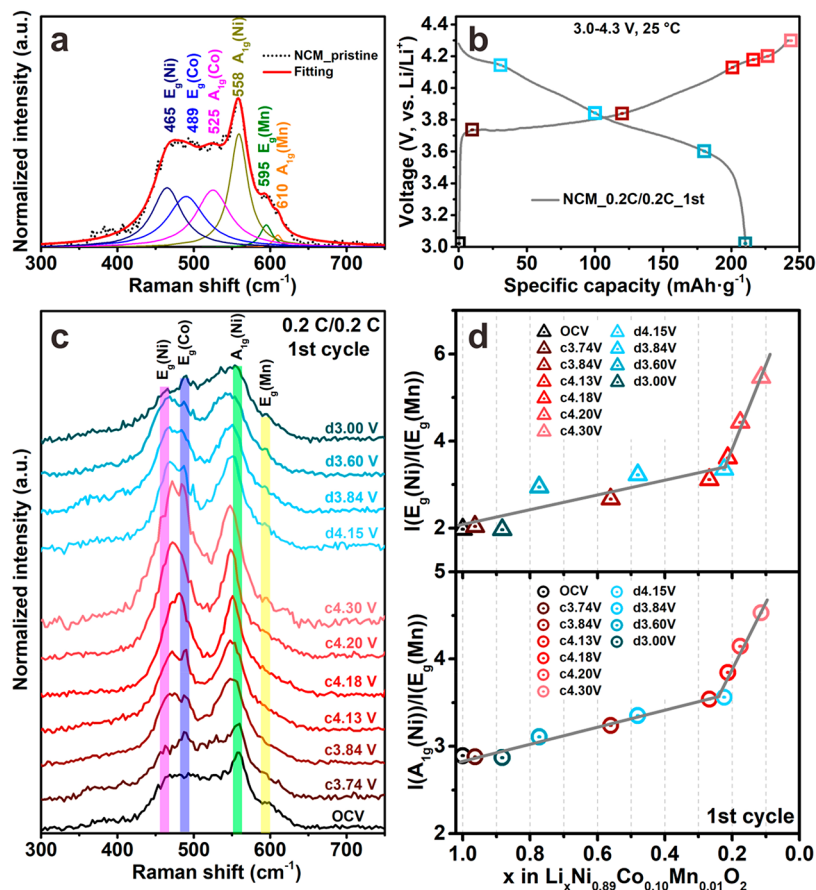


**Figure 2.** (a) Raman spectra of the nickel-rich NCM material and the decomposition of the peak after deconvolution. (b and c) The sample locations and their corresponding Raman spectra of the material during the first cycle at the charging/discharging rate of 0.2 C/0.2 C. (d) The correlation curves between the Raman spectral features of the material and the depth of the redox reaction.

the particle bulk and surface under the low-rate condition ( $t_{0.2\text{ C}} = 18\,000\text{ s}$ ). However, under the high-rate condition ( $t_{10\text{ C}} = 360\text{ s}$ ), lithium ions in the particle bulk may not have enough time to deintercalate from the material compared with those in the surface, and lithium ions intercalated into the particle surface may have no time to diffuse into the bulk sufficiently. Therefore, it is suspected that the severe reaction heterogeneity would occur theoretically within the nickel-rich NCM secondary particle at the high rate rather than the low rate, due to the limitation of the slow solid-phase  $\text{Li}^+$  diffusion and the transient charging/discharging processes.

The basic electrochemical performance of the nickel-rich NCM material is evaluated by cycling coin cells in the voltage region of 3.0–4.3 V at different charging/discharging rates (0.2 C/0.2 C, 0.2 C/10 C, 10 C/0.2, and 10 C/10 C). It is found that the high-rate condition would lead to a large overpotential, causing the decrease in the specific capacity as well as the reaction heterogeneity. First, as shown in Figure 1e and Table S1, the specific capacities during the constant-current charging/discharging steps under the high-rate conditions are obviously lower than those under the low-rate conditions. Second, owing to the limitation of the slow solid-phase  $\text{Li}^+$  diffusion, the overpotential at the high rate is much larger than that at the low rate, thus leading to the significant changes in the redox peaks during the phase transition process (H1–M–H2–H3) in the differential capacity curves (Figure 1f).<sup>2,12,42</sup> Therefore, it is suspected that the large overpotential not only leads to the above-mentioned decrease in the specific capacity

during the constant-current charging/discharging step but also may provide the driving force for the heterogeneous reaction within the nickel-rich NCM secondary particle.

As reported by previous studies, there are two types of Raman-active modes in the nickel-rich NCM materials:  $A_{1g}$ , caused by the stretching vibration of the M–O ( $M = \text{Ni}, \text{Co}, \text{Mn}$ ) bond, and  $E_g$ , arising from the bending vibration of the O–M–O bond. During the charging/discharging process, the redox reaction of  $\text{Ni}^{2+}/\text{Ni}^{4+}$  would result in the change in the local  $\text{MO}_6$  coordination structure, thus causing the variation in the peak intensity/position of the  $A_{1g}$  and  $E_g$  modes.<sup>34–36,40,46</sup> Therefore, in this work, the correlation between the Raman spectral characteristics and the redox reaction depth of the material was established by investigating the change in the  $A_{1g}$  and  $E_g$  modes during the first cycle at the charging/discharging rate of 0.2 C/0.2 C. First, Figure 2a shows the Raman spectra of the pristine nickel-rich NCM material in the range of 400–650  $\text{cm}^{-1}$ , which can be deconvoluted into six Raman-active modes according to previous research:  $A_{1g}(\text{Mn}) \approx 610\text{ cm}^{-1}$ ,  $E_g(\text{Mn}) \approx 595\text{ cm}^{-1}$ ,  $A_{1g}(\text{Ni}) \approx 558\text{ cm}^{-1}$ ,  $A_{1g}(\text{Co}) \approx 525\text{ cm}^{-1}$ ,  $E_g(\text{Co}) \approx 489\text{ cm}^{-1}$ , and  $E_g(\text{Ni}) \approx 465\text{ cm}^{-1}$ .<sup>47–50</sup> Second, through the Raman spectroscopy measurements in Figure 2b–d, it is found that the values of  $I[A_{1g}(\text{Ni})]/I[E_g(\text{Mn})]$  and  $I[E_g(\text{Ni})]/I[E_g(\text{Mn})]$  increase with  $\text{Li}^+$  deintercalation. With the reintercalation of  $\text{Li}^+$  into the structure, the values gradually return to a state close to those of the initial spectrum. Note that the spectrum after discharge to 3.0 V is more similar to that charged to 3.74 V rather than

the pristine state (Figure 2c), indicating the irreversible structural evolution during the first charging/discharging cycle (~85% first-cycle Coulombic efficiency). Therefore, it can be concluded that the greater the values of  $I[A_{1g}(\text{Ni})]/I[E_g(\text{Mn})]$  and  $I[E_g(\text{Ni})]/I[E_g(\text{Mn})]$ , the higher the oxidation reaction depth or the lower the reduction reaction depth.

To analyze the particle-scale reaction heterogeneity, the nickel-rich NCM secondary particles after cycling at different charging/discharging rates are cut to expose the cross sections for further Raman spectroscopy measurements, as shown in Figure 3, parts a and b. Different nickel-rich NCM particles are

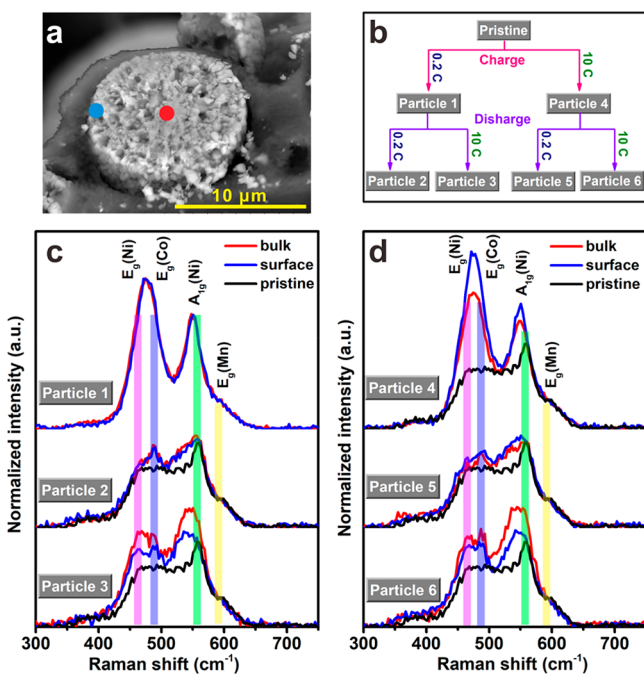


**Figure 3.** (a) SEM image of the cross section of the nickel-rich NCM particle and the test sites of the surface (the blue spot) and bulk (the red spot) structures for Raman spectroscopy measurements. (b–d) The schematic diagram of the charging/discharging rates performed on different particles and the corresponding Raman spectra of the bulk and surface structure.

charged to 4.3 V at 0.2 C (particle 1) or 10 C (particle 4), and then discharged to 3.0 V at 0.2 C (particles 2 and 5) or 10 C (particles 3 and 6), respectively. It is found that the redox reaction is homogeneous within the secondary particle at the low rate, while the redox reaction depth in the particle surface is much higher than that in the particle bulk under the high-rate conditions. First, for the pristine nickel-rich NCM particle (Figure S3a), the Raman spectrum of the particle surface is consistent with that of the bulk, indicating a similar composition of the local  $\text{MO}_6$  coordination structure. Considering the result in Figure S1, parts c and d, it can be declared that the nickel-rich NCM material used in this work has a homogeneous composition. Second, parts c and d of Figure 3 present the Raman spectra of the bulk and surface structure within different particles in Figure 3b. After the low-rate charge (particle 1) and discharge (particles 2 and 5), no significant difference appears in the  $I[A_{1g}(\text{Ni})]/I[E_g(\text{Mn})]$  and  $I[E_g(\text{Ni})]/I[E_g(\text{Mn})]$  values between the surface and bulk structure. However, after the high-rate charge (particle 4)/discharge (particles 3 and 6), the values of the particle surface are obviously larger/smaller than those of the particle bulk.

According to the result in Figure 2, this indicates a higher redox reaction depth of the particle surface than that of the particle bulk under the high-rate condition, which can be attributed to the limitations of the slow solid-phase  $\text{Li}^+$  diffusion and the transient charging/discharging processes. Therefore, it is speculated that, under the high-rate charging/discharging conditions, the redox reaction depth of the particle surface is much higher than that of the particle bulk, different from the homogeneous reaction under the low-rate conditions.

To explicitly confirm the above-mentioned speculation about the particle-scale reaction heterogeneity, the line scanning mode of Raman imaging is performed along the radial direction of the cross sections of different nickel-rich NCM secondary particles in Figure 3b. Figure 4 exhibits the

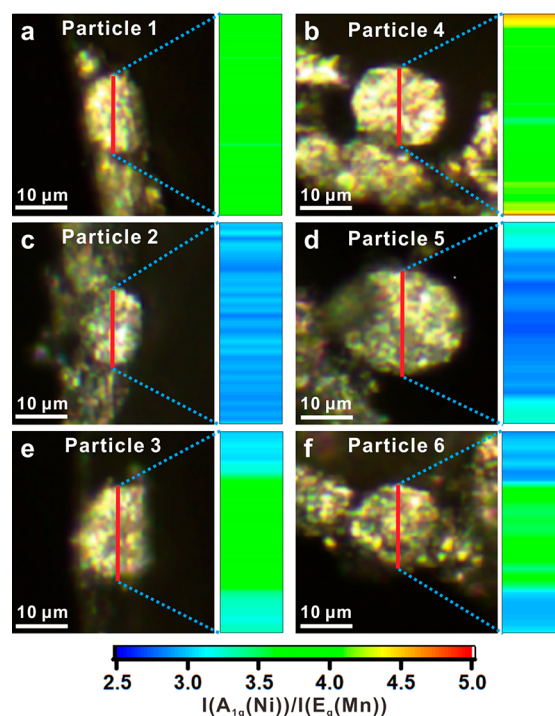


**Figure 4.** Optical images of the cross sections of the nickel-rich NCM secondary particles at different charge/discharge states in Figure 3b and the contour maps of the Raman spectral  $I[A_{1g}(\text{Ni})]/I[E_g(\text{Mn})]$  values along the red line: (a) 0.2 C-charged particle 1, (b) 10 C-charged particle 4, (c) 0.2 C-charged and 0.2 C-discharged particle 2, (d) 10 C-charged and 0.2 C-discharged particle 5, (e) 0.2 C-charged and 10 C-discharged particle 3, and (f) 10 C-charged and 10 C-discharged particle 6.

corresponding contour maps of the Raman spectral  $I[A_{1g}(\text{Ni})]/I[E_g(\text{Mn})]$  values. First, in Figure S3b, the distribution of the  $I[A_{1g}(\text{Ni})]/I[E_g(\text{Mn})]$  value is homogeneous within the pristine particle, which indicates a uniform distribution of the local  $\text{MO}_6$  coordination structure and further confirms the homogeneous composition of the pristine material. Second, during the low-rate charging/discharging processes (Figure 4, parts a, c, and d), the  $I[A_{1g}(\text{Ni})]/I[E_g(\text{Mn})]$  values increase/decrease homogeneously in both the bulk and surface regions of the particles. However, during the high-rate charging process (Figure 4b), the value increase of the particle surface (a depth of 3–4  $\mu\text{m}$  from the outermost surface to the inner bulk) is much larger than that of the particle bulk. Even more, after the high-rate discharge (Figure 4, parts e and f), the value of the particle bulk remains nearly

unchanged. Note that the slight difference in the  $I[A_{1g}(\text{Ni})]/I[E_g(\text{Mn})]$  value between the particle surface and bulk in Figure 4d can be attributed to the overoxidation of the surface after the high-rate charge in Figure 4b. Therefore, it can be verified that the redox reaction mainly occurs in the surface region of the secondary particle under the high-rate conditions, different from the homogeneous redox reaction at the low-rate conditions. This is consistent with the theoretical speculation in Figure 1.

The influence of the particle-scale reaction heterogeneity on the structural stability of the nickel-rich NCM material is further detected by means of XRD and SEM. It is found that the heterogeneous reaction would aggravate the bulk structural instability of the material significantly and lead to particle pulverization. First, parts a–e of Figure 5 present the XRD profiles of the nickel-rich NCM material after 50 cycles at different charging/discharging rates. The  $(311)_{\text{Al}}$  peak at  $78.306^\circ$  is used to correct the peak position in the XRD profiles (Figure 5e). Obviously, all the cycled samples show the typical  $\alpha\text{-NaFeO}_2$ -type layered structure (Figure 5a), and the clear splitting of the  $(006)/(102)$  and  $(108)/(110)$  peaks

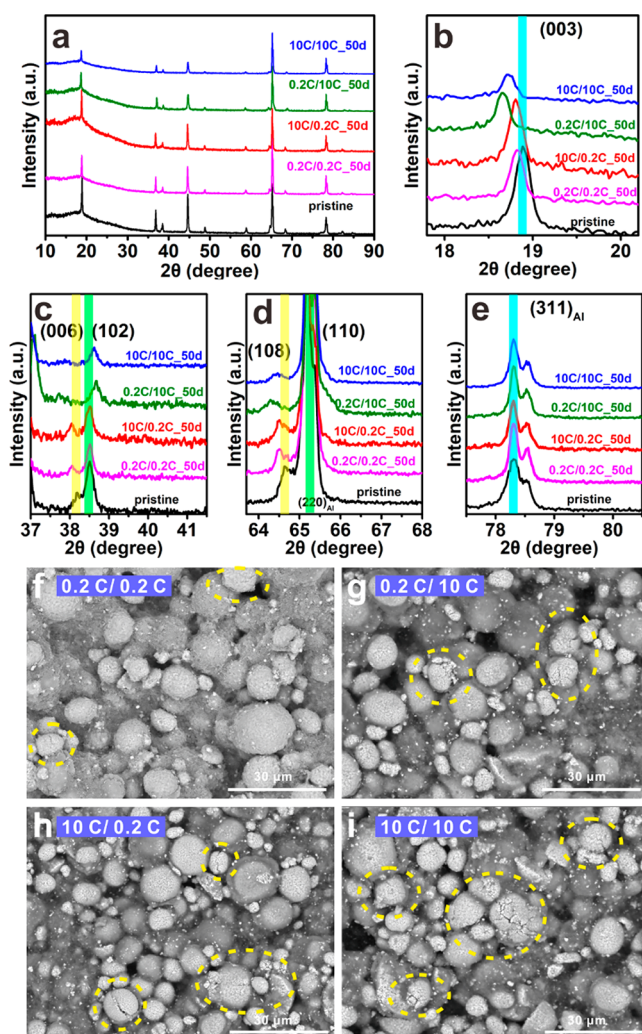


**Figure 5.** (a–e) XRD patterns of the fully discharged nickel-rich NCM materials after 50 cycles at different charging/discharging rates. The SEM images of the nickel-rich NCM electrodes after 50 cycles at different charging/discharging rates: (f) 0.2 C/0.2 C, (g) 0.2 C/10 C, (h) 10 C/0.2 C, and (i) 10 C/10 C.

indicates that the bulk of all the samples maintains a good layered structure before and after cycling (Figure 5, parts c and d).<sup>9,51,52</sup> However, it is worth noting that the  $(003)$ ,  $(006)$ , and  $(108)$  peak positions all shift to a low angle, while the  $(102)$  and  $(110)$  peak positions slightly shift to a high angle after cycling (Figure 5b–d). This indicates an irreversible structure evolution caused by the insufficient intercalation of  $\text{Li}^+$ , which may degrade the structural stability of the material after cycling.<sup>53,54</sup> And the most negative peak shift of the sample under the 0.2 C/10 C condition may imply the worst structural stability during cycling. Second, in order to further confirm the bulk structural stability of the material, the SEM images of the cycled nickel-rich NCM electrodes are obtained. As shown in Figure S4 and Figure 5f–i, severe particle pulverization appears after cycling under the 0.2 C/10 C, 10 C/0.2 C, and 10 C/10 C conditions, rather than the 0.2 C/0.2 C condition. This can be attributed to the aggravated anisotropic stress within the secondary particles caused by the above-mentioned reaction heterogeneity in Figure 4.<sup>41,42</sup> Therefore, it is supposed that the particle-scale reaction heterogeneity would aggravate the particle pulverization at the high-rate charging/discharging conditions. On the one hand, it would lead to the loss of electrical connectivity and affect the reversibility of  $\text{Li}^+$  de/intercalation. On the other hand, the electrolyte penetration into the particle bulk can be promoted, thus accelerating the electrolyte damage on the inner surface of the particles.

The deterioration degree of the surface structure of the cycled nickel-rich NCM materials is evaluated by high-resolution TEM (HR-TEM), as shown in Figure 6. It is

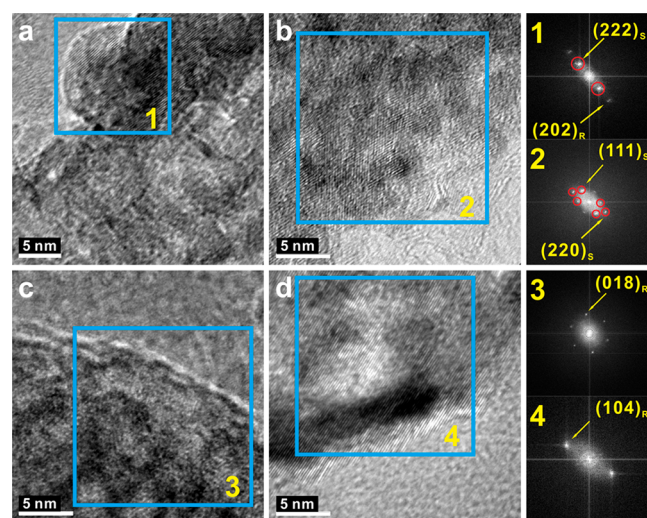


**Figure 6.** HR-TEM images of the nickel-rich NCM material after 50 cycles at different charging/discharging rates and the fast Fourier transform (FFT) images of the selected region: (a) 0.2 C/0.2 C, (b) 0.2 C/10 C, (c) 10 C/0.2 C, and (d) 10 C/10 C. (R represents the layered structure; S represents the spinel structure.)

found that, although the surface structural degradation is caused by the long-term charging process at high potentials, it can be obviously aggravated by the heterogeneous reduction reaction during the high-rate discharging process. First, the surface of the pristine material has the layered structure belonging to the  $R\bar{3}m$  space group (Figure S5). Second, in Figure 6, parts a and b, the spinel structure ( $Fd\bar{3}m$ ) appears in the partial region of the material surface and expands to a large

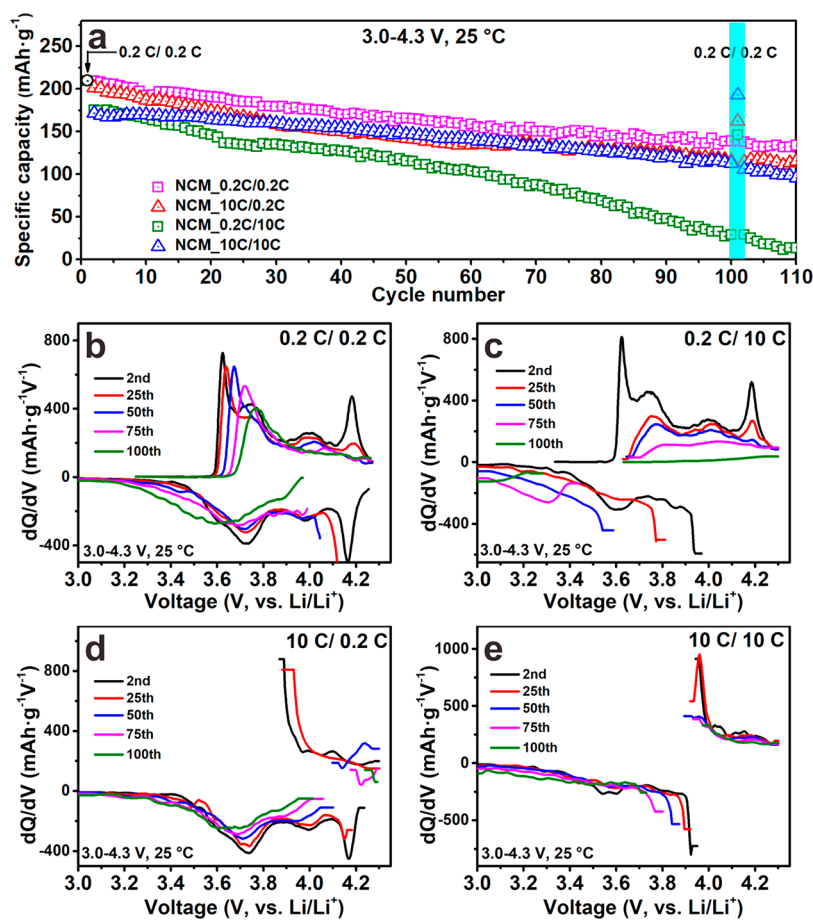


**Figure 7.** (a) Cycle performances of the nickel-rich NCM material at different charging/discharging rates in the voltage region of 3.0–4.3 V and their corresponding differential capacity curves: (b) 0.2 C/0.2 C, (c) 0.2 C/10 C, (d) 10 C/0.2 C, and (e) 10 C/10 C.

scale significantly after cycling under the 0.2 C/0.2 C and 0.2 C/10 C conditions, respectively. The spinel structure is produced by the parasitic reaction between the electrolyte and the highly delithiated surface structure at high potentials.<sup>11,53,55</sup> However, in Figure 6, parts c and d, even after cycling under the conditions of 10 C/0.2 C and 10 C/10 C, the material surface still maintains the layered structure ( $R\bar{3}m$ ). Note that the oxidation depth of the surface structure is much higher under the high-rate charging condition (Figure 4, parts a and b), so it seems to be that the long charging time at high potentials would be another key factor leading to the surface structural degradation, besides the high delithiation degree of the surface structure. Third, in Figure 6, parts a and b, the surface structural degradation under the 0.2 C/10 C condition is much more severe than that under the 0.2 C/0.2 C condition, which may be ascribed to the following two reasons. (i) The heterogeneous reduction reaction under the high-rate discharging condition leads to a lower lithiation degree of the surface structure compared with that under the low-rate discharging condition (Figure 4, parts c and e), which would be in a higher delithiation degree during the subsequent charging process and react with the electrolyte more easily. (ii) The microcracks (Figure 5g) and the much lower lithiation degree of the bulk structure (Figure 4e) caused by the heterogeneous reduction reaction may make the structural degradation expand into the bulk more easily. As reported by the previous study, the reaction heterogeneity and the surface degradation would mutually modulate over time.<sup>56</sup> On the one

hand, as shown in Figure 6, parts a and b, the heterogeneous reaction at the high-rate discharging condition would aggravate the expansion of the surface structural passivation. On the other hand, the partial surface degradation, which is inert to  $\text{Li}^+$  de/intercalation, may in turn affect the evolution of the reaction heterogeneity along the particle surface as well as within the particle. As can be testified in Figure S10, after cycling at the 0.2 C/10 C condition, the oxidation depth of the particle bulk becomes smaller than that of the particle surface, which is quite different from the homogeneous oxidation reaction within the particle after the initial 0.2 C charge in Figure 4a. Therefore, it can be concluded that the long-term charging process at high potentials would be another important factor leading to the surface structural degradation besides the high delithiation degree of the surface structure. Especially in the subsequent high-rate discharging process, the heterogeneous reduction reaction will greatly aggravate the degradation of the surface structure. In addition, the surface structural degradation may in turn affect the evolution of the reaction heterogeneity over time.

The cycle performance of the material is further evaluated by cycling the nickel-rich NCM coin cells at different charging/discharging rates in the voltage region of 3.0–4.3 V, which indicates that the kinetic degradation of  $\text{Li}^+$  is a key factor for the apparent capacity decay. First, as shown in Figure 7a and Table S2, the capacity fading becomes serious when the charging/discharging rate changes from 0.2 C/0.2 C to 0.2 C/10 C, 10 C/0.2 C, and 10 C/10 C. The capacity retention after

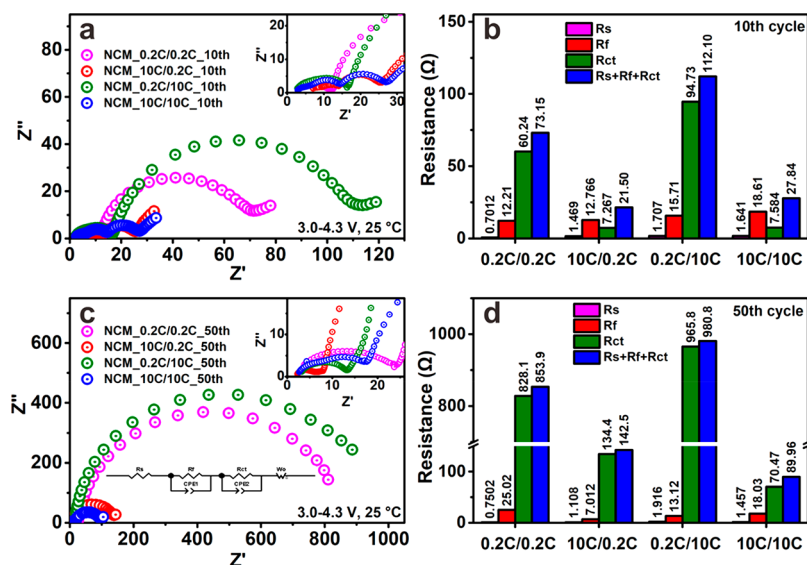


**Figure 8.** EIS profiles of the fully charged nickel-rich NCM coin cells after (a and b) 10 and (c and d) 50 cycles at different charging/discharging rates. The inset in panel c shows the equivalent circuit diagram of the electrode.  $R_s$  is the solution resistance,  $R_f$  is the surface film resistance,  $R_{ct}$  is the interfacial charge-transfer impedance, and  $W_o$  is the Warburg impedance.

100 cycles drops from 66.4% to 16.7%, 57.3%, and 65.8%, respectively. Note that the worst cycle performance under the 0.2 C/10 C condition is consistent with its worst structural stability in Figures 5b and 6b. Second, in the differential capacity curves (Figure 7b–e), the decayed intensity and the increased potential difference of the redox peaks can be observed. This not only is related to the degraded structure stability of the material but also indicates an aggravating electrode polarization during cycling.<sup>6,13,42</sup> As evidenced in Figure S6, the increased electrode polarization would gradually reduce the depth of both the oxidation and reduction reactions of the nickel-rich NCM material and lead to capacity decay. Third, in Figure 7a, the decreased capacities under the 0.2 C/10 C, 10 C/0.2 C, and 10 C/10 C conditions can be restored to 146.3, 162.4, and 193.2 mAh·g<sup>-1</sup>, respectively, after one subsequent charging/discharging cycle at 0.2 C/0.2 C. Interestingly, when the charging/discharging rates return to the initial value, the capacities reduce to their original level again. Therefore, it is indicated that the apparent capacity decay of the nickel-rich NCM material originates mainly from the kinetic degradation of Li<sup>+</sup> de/intercalation during cycling at different charging/discharging rates.

To confirm the connection between the structural degradation of the material and the above-mentioned kinetic deterioration of Li<sup>+</sup> de/intercalation, the impedance changes within the nickel-rich NCM coin cells during cycling are tested by EIS measurements. It is found that the structural degradation of the nickel-rich NCM material would deteriorate the Li<sup>+</sup> kinetics through increasing the interfacial charge-transfer resistance. First, after 10 cycles (Figure 8, parts a and b), no significant difference appears in the solution resistance ( $R_s$ , the intercept on the real axis at the high-frequency region) and the surface film resistance ( $R_f$ , the semicircle in the high-frequency region), but the interfacial charge-transfer resistance ( $R_{ct}$ , the semicircle in the midfrequency region<sup>57,58</sup>) of the 0.2 C/0.2 C and 0.2 C/10 C samples (60.24 and 94.73 Ω) is much larger than that of the 10 C/0.2 C and 10 C/10 C samples (7.267 and 7.584 Ω). Second, after 50 cycles (Figure 8, parts c and d), there is no significant increase in the  $R_s$  and  $R_f$  of all the

samples. Meanwhile, as shown in Figure S7, the capacities of the cycled coin cells cannot recover after rinsing the cycled electrodes with DMC and renewing the electrolyte. It seems to be indicated that the decomposition of the electrolyte is not closely related to kinetic degradation of Li<sup>+</sup>. However, the  $R_{ct}$  of all the samples increases substantially, which can be ascribed to the loss of electrical connectivity caused by the particle pulverization of the material (Figure 5). Third, the much larger  $R_{ct}$  of the 0.2 C/0.2 C and 0.2 C/10 C samples (828.1 and 965.8 Ω) than that of the 10 C/0.2 C and 10 C/10 C samples (134.4 and 70.47 Ω) may be caused by the surface structural degradation as shown in Figure 6, parts a and b. The largest  $R_{ct}$  of the 0.2 C/10 C sample further confirms that, under the high-rate discharging condition, the heterogeneous reduction reaction will significantly aggravate the deterioration of the surface structure. Therefore, it is believed that the structural degradation of the nickel-rich NCM materials aggravated by the reaction heterogeneity would significantly degrade the kinetics of Li<sup>+</sup> de/intercalation at the cathode side and lead to the apparent capacity decay. In addition, the connection between the lithium metal anode and the kinetic degradation of Li<sup>+</sup> is further discussed in Figure S8, which indicates that the kinetic degradation at the anode side under the high-rate charging conditions is more obvious than that under the low-rate charging conditions. Considering all the results obtained, it is suggested that the electrochemical operating conditions of the nickel-rich NCM batteries should be designed rationally. For example, avoid using the batteries under low-rate charging/high-rate discharging conditions. The charging rate should not be either too low or too high to avoid the severe surface structural degradation of the materials or anode degradation. For the purpose of the high-rate charge/discharge, one should be on the alert for particle pulverization caused by the reaction heterogeneity.

#### 4. CONCLUSIONS

In this work, the particle-scale reaction heterogeneity of nickel-rich NCM material and its influence on the structure and cycle stability are systematically investigated. It is found that the

reaction heterogeneity is significantly affected by the electrochemical operating conditions of the nickel-rich NCM materials and would aggravate the structural degradation as well as the capacity decay.

First, Raman spectroscopy is applied to conveniently conduct the high-resolution and in-depth analysis of the rate-dependent redox heterogeneity within the nickel-rich NCM secondary particles. It is found that the redox reaction mainly occurs in the surface region of the secondary particle under the high-rate condition (10 C), different from the homogeneous reaction under the low-rate condition (0.2 C). As estimated by the GITT measurements, the cause of this particle-scale reaction heterogeneity seems to be the limitation of the slow solid-phase diffusion of  $\text{Li}^+$  and the transient charging/discharging processes under the high-rate condition. Second, the structural characterization measurements (XRD, SEM, and HR-TEM) show that the reaction heterogeneity would aggravate the particle pulverization of the material during cycling. Besides the high delithiation degree of the surface structure, the long-term charging process at high potentials would be another important factor leading to the surface structural degradation. Especially in the subsequent high-rate discharging process, the heterogeneous reduction reaction will greatly aggravate the degradation of the surface structure. Third, as indicated by the electrochemical measurements, the structural degradation of the material would lead to the kinetic degradation of  $\text{Li}^+$  de/intercalation at the cathode side, which may be a key factor for the apparent capacity decay during long-term cycles.

Through our comprehensive investigation on the particle-scale reaction heterogeneity, it can be realized that boosting the homogeneous reaction within the material particles is of great significance for achieving high-power LIBs. In the aspect of the material preparation, the concentration-gradient or element-doping methods may be helpful to adjust the reaction heterogeneity or accelerate the solid-phase  $\text{Li}^+$  diffusion at the high-rate condition, and the single-crystal strategy is useful to avoid particle pulverization. For the design of the electrochemical operating conditions, the low-rate charging/high-rate discharging conditions should be avoided and the charging rate should not be either too low or too high to avoid severe surface structural degradation of the materials or anode deterioration.

## ■ ASSOCIATED CONTENT

### SI Supporting Information

The Supporting Information is available free of charge at <https://pubs.acs.org/doi/10.1021/acsami.1c05819>.

XRD, SEM, TEM, and Raman spectra patterns of the pristine nickel-rich material, calculation processes of the solid-phase  $\text{Li}^+$  diffusion coefficient and lithium ionic conductivity, Raman spectra of the surface structure after 50 cycles, cycle performances of the reassembled half-cells, SEM patterns of the lithium metal anodes after 50 cycles, proof of the elimination of the electrode-scale reaction heterogeneity, mutual modulation of the surface degradation and reaction heterogeneity, and quantitative analysis of reaction heterogeneity (PDF)

## ■ AUTHOR INFORMATION

### Corresponding Authors

Xue Li – Faculty of Metallurgical and Energy Engineering, Kunming University of Science and Technology, Kunming

650093, People's Republic of China; Email: 438616074@qq.com

Jinbao Zhao – College of Chemistry and Chemical Engineering, Xiamen University, Xiamen 361005, People's Republic of China; [orcid.org/0000-0002-2753-7508](https://orcid.org/0000-0002-2753-7508); Email: jbzha@xmu.edu.cn

### Authors

Jiyang Li – College of Chemistry and Chemical Engineering, Xiamen University, Xiamen 361005, People's Republic of China

Jingxin Huang – College of Chemistry and Chemical Engineering, Xiamen University, Xiamen 361005, People's Republic of China

Hongyang Li – College of Chemistry and Chemical Engineering, Xiamen University, Xiamen 361005, People's Republic of China

Xiangbang Kong – College of Chemistry and Chemical Engineering, Xiamen University, Xiamen 361005, People's Republic of China

Complete contact information is available at: <https://pubs.acs.org/doi/10.1021/acsami.1c05819>

### Notes

The authors declare no competing financial interest.

## ■ ACKNOWLEDGMENTS

We gratefully acknowledge the financial support of National Key Research and Development Program of China [2017YFB0102000], the National Natural Science Foundation of China [21965017, 22021001], and the Key Project of Science and Technology of Xiamen [3502Z20201013]. The authors also want to express their gratitude to Dr. Chuan Liu from the College of Chemistry and Chemical Engineering in Xiamen University for his kind help on Raman spectroscopy measurements.

## ■ REFERENCES

- (1) Chakraborty, A.; Kunnikuruvaan, S.; Kumar, S.; Markovsky, B.; Aurbach, D.; Dixit, M.; Major, D. T. Layered Cathode Materials for Lithium-Ion Batteries: Review of Computational Studies on  $\text{LiNi}_{1-x-y}\text{Co}_x\text{Mn}_y\text{O}_2$  and  $\text{LiNi}_{1-x-y}\text{Co}_x\text{Al}_y\text{O}_2$ . *Chem. Mater.* **2020**, *32* (3), 915–952.
- (2) Song, S. H.; Cho, M.; Park, I.; Yoo, J.-G.; Ko, K.-T.; Hong, J.; Kim, J.; Jung, S.-K.; Avdeev, M.; Ji, S.; Lee, S.; Bang, J.; Kim, H. High-Voltage-Driven Surface Structuring and Electrochemical Stabilization of Ni-Rich Layered Cathode Materials for Li Rechargeable Batteries. *Adv. Energy Mater.* **2020**, *10* (23), 2000521.
- (3) Zhang, X.-D.; Shi, J.-L.; Liang, J.-Y.; Yin, Y.-X.; Zhang, J.-N.; Yu, X.-Q.; Guo, Y.-G. Suppressing Surface Lattice Oxygen Release of Li-Rich Cathode Materials via Heterostructured Spinel  $\text{Li}_4\text{Mn}_5\text{O}_{12}$  Coating. *Adv. Mater.* **2018**, *30*, 1801751.
- (4) Shi, J.-L.; Xiao, D.-D.; Zhang, X.-D.; Yin, Y.-X.; Guo, Y.-G.; Gu, L.; Wan, L.-J. Improving the Structural Stability of Li-Rich Cathode Materials via Reservation of Cations in the Li-Slab for Li-Ion Batteries. *Nano Res.* **2017**, *10* (12), 4201–4209.
- (5) Wang, X.; Ding, Y.-L.; Deng, Y.-P.; Chen, Z. Ni-Rich/Co-Poor Layered Cathode for Automotive Li-Ion Batteries: Promises and Challenges. *Adv. Energy Mater.* **2020**, *10* (12), 1903864.
- (6) Han, Y.; Heng, S.; Wang, Y.; Qu, Q.; Zheng, H. Anchoring Interfacial Nickel Cations on Single Crystal  $\text{LiNi}_{0.8}\text{Co}_{0.1}\text{Mn}_{0.1}\text{O}_2$  Cathode Surface via Controllable Electron Transfer. *ACS Energy Letters* **2020**, *5*, 2421–2433.
- (7) Xu, G.-L.; Liu, Q.; Lau, K. K. S.; Liu, Y.; Liu, X.; Gao, H.; Zhou, X.; Zhuang, M.; Ren, Y.; Li, J.; Shao, M.; Ouyang, M.; Pan, F.; Chen,

Z.; Amine, K.; Chen, G. Building Ultraconformal Protective Layers on Both Secondary and Primary Particles of Layered Lithium Transition Metal Oxide Cathodes. *Nature Energy* **2019**, *4* (6), 484–494.

(8) Liu, X.; Xu, G.-L.; Yin, L.; Hwang, I.; Li, Y.; Lu, L.; Xu, W.; Zhang, X.; Chen, Y.; Ren, Y.; Sun, C.-J.; Chen, Z.; Ouyang, M.; Amine, K. Probing the Thermal-Driven Structural and Chemical Degradation of Ni-Rich Layered Cathodes by Co/Mn Exchange. *J. Am. Chem. Soc.* **2020**, *142* (46), 19745–19753.

(9) Chen, Z.; Wang, J.; Huang, J.; Fu, T.; Sun, G.; Lai, S.; Zhou, R.; Li, K.; Zhao, J. The High-Temperature and High-Humidity Storage Behaviors and Electrochemical Degradation Mechanism of LiNi<sub>0.6</sub>Co<sub>0.2</sub>Mn<sub>0.2</sub>O<sub>2</sub> Cathode Material for Lithium Ion Batteries. *J. Power Sources* **2017**, *363*, 168–176.

(10) Yan, P.; Zheng, J.; Chen, T.; Luo, L.; Jiang, Y.; Wang, K.; Sui, M.; Zhang, J.-G.; Zhang, S.; Wang, C. Coupling of Electrochemically Triggered Thermal and Mechanical Effects to Aggravate Failure in a Layered Cathode. *Nat. Commun.* **2018**, *9* (1), 2437.

(11) Xu, C.; Märker, K.; Lee, J.; Mehdi, B. L.; Mahadevegowda, A.; Reeves, P. J.; Day, S. J.; Groh, M. F.; Emge, S. P.; Ducati, C.; et al. Bulk Fatigue Induced by Surface Reconstruction in Layered Ni-Rich Cathodes for Li-Ion Batteries. *Nat. Mater.* **2021**, *20* (1), 84–92.

(12) Ko, D.-S.; Park, J.-H.; Yu, B. Y.; Ahn, D.; Kim, K.; Han, H. N.; Jeon, W. S.; Jung, C.; Manthiram, A. Degradation of High-Nickel-Layered Oxide Cathodes from Surface to Bulk: A Comprehensive Structural, Chemical, and Electrical Analysis. *Adv. Energy Mater.* **2020**, *10* (36), 2001035.

(13) Noh, H.-J.; Yoon, S.; Yoon, C. S.; Sun, Y.-K. Comparison of the Structural and Electrochemical Properties of Layered Li-[Ni<sub>x</sub>CoyMnz]O<sub>2</sub> (x = 1/3, 0.5, 0.6, 0.7, 0.8 and 0.85) Cathode Material for Lithium-Ion Batteries. *J. Power Sources* **2013**, *233*, 121–130.

(14) Bak, S.-M.; Hu, E.; Zhou, Y.; Yu, X.; Senanayake, S. D.; Cho, S.-J.; Kim, K.-B.; Chung, K. Y.; Yang, X.-Q.; Nam, K.-W. Structural Changes and Thermal Stability of Charged LiNi<sub>x</sub>MnyCozO<sub>2</sub> Cathode Materials Studied by Combined In Situ Time-Resolved XRD and Mass Spectroscopy. *ACS Appl. Mater. Interfaces* **2014**, *6* (24), 22594–22601.

(15) Lim, B.-B.; Myung, S.-T.; Yoon, C. S.; Sun, Y.-K. Comparative Study of Ni-Rich Layered Cathodes for Rechargeable Lithium Batteries: Li[Ni<sub>0.85</sub>Co<sub>0.11</sub>Al<sub>0.04</sub>]O<sub>2</sub> and Li-[Ni<sub>0.84</sub>Co<sub>0.06</sub>Mn<sub>0.09</sub>Al<sub>0.01</sub>]O<sub>2</sub> with Two-Step Full Concentration Gradients. *ACS Energy Letters* **2016**, *1* (1), 283–289.

(16) Kim, U.-H.; Lee, E.-J.; Yoon, C. S.; Myung, S.-T.; Sun, Y.-K. Compositionally Graded Cathode Material with Long-Term Cycling Stability for Electric Vehicles Application. *Adv. Energy Mater.* **2016**, *6* (22), 1601417.

(17) Sun, Y.-K.; Myung, S.-T.; Park, B.-C.; Prakash, J.; Belharouak, I.; Amine, K. High-Energy Cathode Material for Long-Life and Safe Lithium Batteries. *Nat. Mater.* **2009**, *8* (4), 320–324.

(18) Hua, W.; Schwarz, B.; Azmi, R.; Müller, M.; Dewi Darma, M. S.; Knapp, M.; Senyshyn, A.; Heere, M.; Missyul, A.; Simonelli, L.; Binder, J. R.; Indris, S.; Ehrenberg, H. Lithium-Ion (De)intercalation Mechanism in Core-Shell Layered Li(Ni,Co, Mn)O<sub>2</sub> Cathode Materials. *Nano Energy* **2020**, *78*, 105231.

(19) Jow, T. R.; Delp, S. A.; Allen, J. L.; Jones, J.-P.; Smart, M. C. Factors Limiting Li<sup>+</sup> Charge Transfer Kinetics in Li-Ion Batteries. *J. Electrochem. Soc.* **2018**, *165* (2), A361–A367.

(20) Ho, C.; Raistrick, I. D.; Huggins, R. A. Application of A-C Techniques to the Study of Lithium Diffusion in Tungsten Trioxide Thin Films. *J. Electrochem. Soc.* **1980**, *127*, 343–350.

(21) Shaju, K. M.; Subba Rao, G. V.; Chowdari, B. V. R. EIS and GITT Studies on Oxide Cathodes, O<sub>2</sub>-Li(2/3)+x(Co<sub>0.15</sub>Mn<sub>0.85</sub>)O<sub>2</sub> (x = 0 and 1/3). *Electrochim. Acta* **2003**, *48* (18), 2691–2703.

(22) Smith, K.; Wang, C.-Y. Solid-State Diffusion Limitations on Pulse Operation of a Lithium Ion Cell for Hybrid Electric Vehicles. *J. Power Sources* **2006**, *161* (1), 628–639.

(23) Nara, H.; Morita, K.; Mukoyama, D.; Yokoshima, T.; Momma, T.; Osaka, T. Impedance Analysis of LiNi<sub>1/3</sub>Mn<sub>1/3</sub>Co<sub>1/3</sub>O<sub>2</sub>

Cathodes with Different Secondary-Particle Size Distribution in Lithium-Ion Battery. *Electrochim. Acta* **2017**, *241*, 323–330.

(24) Orikasa, Y.; Gogyo, Y.; Yamashige, H.; Katayama, M.; Chen, K.; Mori, T.; Yamamoto, K.; Masese, T.; Inada, Y.; Ohta, T.; et al. Ionic Conduction in Lithium Ion Battery Composite Electrode Governs Cross-Sectional Reaction Distribution. *Sci. Rep.* **2016**, *6*, 26382.

(25) Wei, C.; Xia, S.; Huang, H.; Mao, Y.; Pianetta, P.; Liu, Y. Mesoscale Battery Science: The Behavior of Electrode Particles Caught on a Multispectral X-ray Camera. *Acc. Chem. Res.* **2018**, *51* (10), 2484–2492.

(26) Yang, Y.; Xu, R.; Zhang, K.; Lee, S.-J.; Mu, L.; Liu, P.; Waters, C. K.; Spence, S.; Xu, Z.; Wei, C.; Kautz, D. J.; Yuan, Q.; Dong, Y.; Yu, Y.-S.; Xiao, X.; Lee, H.-K.; Pianetta, P.; Cloetens, P.; Lee, J.-S.; Zhao, K.; Lin, F.; Liu, Y. Quantification of Heterogeneous Degradation in Li-Ion Batteries. *Adv. Energy Mater.* **2019**, *9* (25), 1900674.

(27) Hu, J.; Wu, B.; Cao, X.; Bi, Y.; Chae, S.; Niu, C.; Xiao, B.; Tao, J.; Zhang, J.; Xiao, J. Evolution of the Rate-Limiting Step: from Thin Film to Thick Ni-Rich Cathodes. *J. Power Sources* **2020**, *454*, 227966.

(28) Cha, H.; Kim, J.; Lee, H.; Kim, N.; Hwang, J.; Sung, J.; Yoon, M.; Kim, K.; Cho, J. Boosting Reaction Homogeneity in High-Energy Lithium-Ion Battery Cathode Materials. *Adv. Mater.* **2020**, *32* (39), 2003040.

(29) Zhou, Y.-N.; Yue, J.-L.; Hu, E.; Li, H.; Gu, L.; Nam, K.-W.; Bak, S.-M.; Yu, X.; Liu, J.; Bai, J.; Dooryhee, E.; Fu, Z.-W.; Yang, X.-Q. High-Rate Charging Induced Intermediate Phases and Structural Changes of Layer-Structured Cathode for Lithium-Ion Batteries. *Adv. Energy Mater.* **2016**, *6* (21), 1600597.

(30) Xu, Y.; Hu, E.; Zhang, K.; Wang, X.; Borzenets, V.; Sun, Z.; Pianetta, P.; Yu, X.; Liu, Y.; Yang, X.-Q.; Li, H. In Situ Visualization of State-of-Charge Heterogeneity within a LiCoO<sub>2</sub> Particle that Evolves upon Cycling at Different Rates. *ACS Energy Letters* **2017**, *2* (5), 1240–1245.

(31) Xia, S.; Mu, L.; Xu, Z.; Wang, J.; Wei, C.; Liu, L.; Pianetta, P.; Zhao, K.; Yu, X.; Lin, F.; Liu, Y. Chemomechanical Interplay of Layered Cathode Materials Undergoing Fast Charging in Lithium Batteries. *Nano Energy* **2018**, *53*, 753–762.

(32) Hwang, S.; Jo, E.; Chung, K. Y.; Hwang, K. S.; Kim, S. M.; Chang, W. Structural Evolution of Li<sub>x</sub>NiyMnzCo<sub>1-y-z</sub>O<sub>2</sub> Cathode Materials during High-Rate Charge and Discharge. *J. Phys. Chem. Lett.* **2017**, *8* (23), 5758–5763.

(33) Gong, Z.-L.; Zhang, W.; LV, D.-p.; Hao, X.-g.; Wen, W.; Jiang, Z.; Yang, Y. Application of Synchrotron Radiation Based Electrochemical In-Situ Techniques to Study of Electrode Materials for Lithium-Ion Batteries. *J. Electrochem.* **2013**, *19* (6), 512–522.

(34) Flores, E.; Vonrüti, N.; Novák, P.; Aschauer, U.; Berg, E. J. Elucidation of Li<sub>x</sub>Ni<sub>0.8</sub>Co<sub>0.15</sub>Al<sub>0.05</sub>O<sub>2</sub> Redox Chemistry by Operando Raman Spectroscopy. *Chem. Mater.* **2018**, *30* (14), 4694–4703.

(35) Flores, E.; Novák, P.; Aschauer, U.; Berg, E. J. Cation Ordering and Redox Chemistry of Layered Ni-Rich Li<sub>x</sub>Ni<sub>1-2y</sub>CoyMnyO<sub>2</sub>: An Operando Raman Spectroscopy Study. *Chem. Mater.* **2020**, *32* (1), 186–194.

(36) Huang, J.-X.; Li, B.; Liu, B.; Liu, B.-J.; Zhao, J.-B.; Ren, B. Structural Evolution of NM (Ni and Mn) Lithium-Rich Layered Material Revealed by In-Situ Electrochemical Raman Spectroscopic Study. *J. Power Sources* **2016**, *310*, 85–90.

(37) Lin, M.-H.; Cheng, J.-H.; Huang, H.-F.; Chen, U.-F.; Huang, C.-M.; Hsieh, H.-W.; Lee, J.-M.; Chen, J.-M.; Su, W.-N.; Hwang, B.-J. Revealing the Mitigation of Intrinsic Structure Transformation and Oxygen Evolution in a Layered Li<sub>1.2</sub>Ni<sub>0.2</sub>Mn<sub>0.6</sub>O<sub>2</sub> Cathode Using Restricted Charging Protocols. *J. Power Sources* **2017**, *359*, 539–548.

(38) Nanda, J.; Remillard, J.; O'Neill, A.; Bernardi, D.; Ro, T.; Nietering, K. E.; Go, J.-Y.; Miller, T. J. Local State-of-Charge Mapping of Lithium-Ion Battery Electrodes. *Adv. Funct. Mater.* **2011**, *21* (17), 3282–3290.

(39) Baddour-Hadjean, R.; Pereira-Ramos, J.-P. Raman Microspectrometry Applied to the Study of Electrode Materials for Lithium Batteries. *Chem. Rev.* **2010**, *110* (3), 1278–1319.

- (40) Fang, S.; Yan, M.; Hamers, R. J. Cell Design and Image Analysis for In-Situ Raman Mapping of Inhomogeneous State-of-Charge Profiles in Lithium-Ion Batteries. *J. Power Sources* **2017**, *352*, 18–25.
- (41) Park, K.-J.; Hwang, J.-Y.; Ryu, H.-H.; Maglia, F.; Kim, S.-J.; Lamp, P.; Yoon, C. S.; Sun, Y.-K. Degradation Mechanism of Ni-Enriched NCA Cathode for Lithium Batteries: Are Microcracks Really Critical? *ACS Energy Letters* **2019**, *4*, 1394–1400.
- (42) Kim, U.-H.; Park, N.-Y.; Park, G.-T.; Kim, H.; Yoon, C. S.; Sun, Y.-K. High-Energy W-Doped Li[Ni<sub>0.95</sub>Co<sub>0.04</sub>Al<sub>0.01</sub>]O<sub>2</sub> Cathodes for Next-Generation Electric Vehicles. *Energy Storage Materials* **2020**, *33*, 399–407.
- (43) Ruther, R. E.; Callender, A. F.; Zhou, H.; Martha, S. K.; Nanda, J. Raman Microscopy of Lithium-Manganese-Rich Transition Metal Oxide Cathodes. *J. Electrochem. Soc.* **2015**, *162* (1), A98–A102.
- (44) Weppner, W.; Huggins, R. A. Determination of the Kinetic Parameters of Mixed-Conducting Electrodes and Application to the System Li<sub>3</sub>Sb. *J. Electrochem. Soc.* **1977**, *124* (10), 1569–1578.
- (45) Leftheriotis, G.; Papaefthimiou, S.; Yianoulis, P. Dependence of the Estimated Diffusion Coefficient of Li<sub>x</sub>WO<sub>3</sub> Films on the Scan Rate of Cyclic Voltammetry Experiments. *Solid State Ionics* **2007**, *178* (3–4), 259–263.
- (46) Singh, G.; West, W. C.; Soler, J.; Katiyar, R. S. In Situ Raman Spectroscopy of Layered Solid Solution Li<sub>2</sub>MnO<sub>3</sub>-LiMO<sub>2</sub> (M = Ni, Mn, Co). *J. Power Sources* **2012**, *218*, 34–38.
- (47) Ben-Kamel, K.; Amdouni, N.; Mauger, A.; Julien, C. M. Study of the Local Structure of LiNi<sub>0.33+δ</sub>Mn<sub>0.33+δ</sub>Co<sub>0.33-2δ</sub>O<sub>2</sub> (0.025 ≤ δ ≤ 0.075) Oxides. *J. Alloys Compd.* **2012**, *528*, 91–98.
- (48) Zhang, X.; Mauger, A.; Lu, Q.; Groult, H.; Perrigaud, L.; Gendron, F.; Julien, C. M. Synthesis and Characterization of LiNi<sub>1/3</sub>Mn<sub>1/3</sub>Co<sub>1/3</sub>O<sub>2</sub> by Wet-Chemical Method. *Electrochim. Acta* **2010**, *55* (22), 6440–6449.
- (49) Kong, J.-Z.; Wang, S.-S.; Tai, G.-A.; Zhu, L.; Wang, L.-G.; Zhai, H.-F.; Wu, D.; Li, A.-D.; Li, H. Enhanced Electrochemical Performance of LiNi<sub>0.5</sub>Co<sub>0.2</sub>Mn<sub>0.3</sub>O<sub>2</sub> Cathode Material by Ultrathin ZrO<sub>2</sub> Coating. *J. Alloys Compd.* **2016**, *657*, 593–600.
- (50) Ghanty, C.; Markovsky, B.; Erickson, E. M.; Talianker, M.; Haik, O.; Tal-Yossef, Y.; Mor, A.; Aurbach, D.; Lampert, J.; Volkov, A.; Shin, J.-Y.; Garsuch, A.; Chesneau, F. F.; Erk, C. Li<sup>+</sup>-Ion Extraction/Insertion of Ni-Rich Li<sub>1+x</sub>(Ni<sub>y</sub>Co<sub>z</sub>Mn<sub>z</sub>)<sub>w</sub>O<sub>2</sub> (0.005 < x < 0.03; y:z = 8:1, w ≈ 1) Electrodes: In Situ XRD and Raman Spectroscopy Study. *ChemElectroChem* **2015**, *2* (10), 1479–1486.
- (51) Kong, X.; Peng, S.; Li, J.; Chen, Z.; Chen, Z.; Wang, J.; Zhao, J. Pre-Blended Conductive Agent to Effectively Improve the Storage Properties of LiNi<sub>0.6</sub>Co<sub>0.2</sub>Mn<sub>0.2</sub>O<sub>2</sub> Cathode Materials. *J. Power Sources* **2020**, *448*, 227445.
- (52) Huang, B.; Liu, D.; Qian, K.; Zhang, L.; Zhou, K.; Liu, Y.; Kang, F.; Li, B. A Simple Method for the Complete Performance Recovery of Degraded Ni-Rich LiNi<sub>0.70</sub>Co<sub>0.15</sub>Mn<sub>0.15</sub>O<sub>2</sub> Cathode via Surface Reconstruction. *ACS Appl. Mater. Interfaces* **2019**, *11* (15), 14076–14084.
- (53) Jung, S.-K.; Gwon, H.; Hong, J.; Park, K.-Y.; Seo, D.-H.; Kim, H.; Hyun, J.; Yang, W.; Kang, K. Understanding the Degradation Mechanisms of LiNi<sub>0.5</sub>Co<sub>0.2</sub>Mn<sub>0.3</sub>O<sub>2</sub> Cathode Material in Lithium Ion Batteries. *Adv. Energy Mater.* **2014**, *4* (1), 1300787.
- (54) Lee, S.; Jang, D.; Yoon, J.; Cho, Y.-H.; Lee, Y.-S.; Kim, D.-H.; Kim, W.-S.; Yoon, W.-S. Crystal Structure Changes of LiNi<sub>0.5</sub>Co<sub>0.2</sub>Mn<sub>0.3</sub>O<sub>2</sub> Cathode Materials During the First Charge Investigated by In Situ XRD. *J. Electrochem. Sci. Technol.* **2012**, *3* (1), 29–34.
- (55) Kuriyama, H.; Saruwatari, H.; Satake, H.; Shima, A.; Uesugi, F.; Tanaka, H.; Ushirogouchi, T. Observation of Anisotropic Microstructural Changes during Cycling in LiNi<sub>0.5</sub>Co<sub>0.2</sub>Mn<sub>0.3</sub>O<sub>2</sub> Cathode Material. *J. Power Sources* **2015**, *275*, 99–105.
- (56) Li, S.; Jiang, Z.; Han, J.; Xu, Z.; Wang, C.; Huang, H.; Yu, C.; Lee, S.-J.; Pianetta, P.; Ohldag, H.; et al. Mutual Modulation between Surface Chemistry and Bulk Microstructure within Secondary Particles of Nickel-Rich Layered Oxides. *Nat. Commun.* **2020**, *11* (1), 4433.
- (57) Chen, Z.; Liu, C.; Sun, G.; Kong, X.; Lai, S.; Li, J.; Zhou, R.; Wang, J.; Zhao, J. Electrochemical Degradation Mechanism and Thermal Behaviors of the Stored LiNi<sub>0.5</sub>Co<sub>0.2</sub>Mn<sub>0.3</sub>O<sub>2</sub> Cathode Materials. *ACS Appl. Mater. Interfaces* **2018**, *10* (30), 25454–25464.
- (58) Zhao, X.; Zhuang, Q.-C.; Wu, C.; Wu, K.; Xu, J.-M.; Zhang, M.-Y.; Sun, X.-L. Impedance Studies on the Capacity Fading Mechanism of Li(Ni<sub>0.5</sub>Co<sub>0.2</sub>Mn<sub>0.3</sub>)O<sub>2</sub> Cathode with High-Voltage and High-Temperature. *J. Electrochem. Soc.* **2015**, *162* (14), A2770–A2779.